nature physics

ARTICLES

https://doi.org/10.1038/s41567-021-01492-w

Check for updates

# Topological dissipation in a time-multiplexed photonic resonator network

Christian Leefmans[1,9], Avik Dutt[2,3,9], James Williams[4], Luqi Yuan[5], Midya Parto[4], Franco Nori[6,7,8], Shanhui Fan[2] and Alireza Marandi[1,4]✉

**Topological phases feature robust edge states that are protected against the effects of defects and disorder. These phases have largely been studied in conservatively coupled systems, in which non-trivial topological invariants arise in the energy or frequency bands of a system. Here we show that, in dissipatively coupled systems, non-trivial topological invariants can emerge purely in a system's dissipation. Using a highly scalable and easily reconfigurable time-multiplexed photonic resonator network, we experimentally demonstrate one- and two-dimensional lattices that host robust topological edge states with isolated dissipation rates, measure a dissipation spectrum that possesses a non-trivial topological invariant, and demonst rate topological protection of the network's quality factor. The topologically non-trivial dissipation of our system exposes new opportunities to engineer dissipation in both classical and quantum systems. Moreover, our experimental platform's straightforward scaling to higher dimensions and its ability to implement inhomogeneous, non-reciprocal and long range couplings may enable future work in the study of synthetic dimensions.**

Most topological phases in condensed matter[1], ultracold atoms[2] and photonics[3] rely on conservative couplings to achieve non-trivial topological invariants. Conservative couplings arise when the elements of a system—either atoms of a quantum system or ring resonators of a photonic system (Fig. 1a)—exchange information directly through their overlapping modes. The conservation of energy imposes a particular set of possible phase relationships on conservative couplings due to the unitary nature of the scattering matrix. In topological lattice models, conservative couplings engender energy or frequency spectra whose bands are characterized by quantized, non-zero topological invariants. The presence of non-trivial topological invariants, in turn, gives rise to topologically protected edge states at the boundaries of the lattice[4,5], whose existence is robust against the presence of defects and disorder. The edge states of conservatively coupled systems are touted for their unusual and exceptional transport dynamics, which may be unidirectional and free from backscattering.

Dissipative couplings indirectly couple the elements of a system through an intermediate reservoir[6,7], such as a bath of atomic modes or the modes of a bus waveguide[8] (Fig. 1a). Dissipative couplings may be thought of as two separate couplings: information from one element of the system first couples into the reservoir and then couples from the reservoir into a second element of the system. In general, some information is irrevocably lost to the reservoir in this process, and dissipative couplings do not conserve energy. However, dissipative couplings enable additional freedom to engineer the coupling phases, as the system's scattering matrix is no longer unitary. (It is essential to distinguish dissipative couplings from the on-site gain and loss produced by, say, laser gain and absorption. The latter phenomena, combined with conservative couplings, have been extensively studied in both theory and experiment in non-Hermitian topological photonics. In this work, we study non-trivial topology that appears solely due to dissipative couplings. Such a phenomenon has not been experimentally studied in topological photonics.) As shown in Fig. 1a, the right choice of coupling phases can introduce splittings purely in the dissipation modes of a system. Other coupling phases may introduce splittings in the frequency modes of a system or in a combination of frequency and dissipation modes (Supplementary Section 3). Such 'dissipation engineering' plays an important role in superconducting circuits, ultracold atoms and photonics, where it is used for reservoir engineering[9], laser mode-locking[10,11], and quantum and photonic computing[12–14]. Several recent studies have proposed combining dissipative and conservative couplings to enable time-reversal symmetry-breaking couplings[15] and to induce non-trivial topological invariants[16–20]. These proposals suggest that dissipative coupling, like nonlinearity[21–23] and local gain and loss[24–26], may enable new topological phases and topology-inspired technologies for quantum and classical applications. However, topological phases that arise in lattices with purely dissipative couplings remain largely unexplored[27,28].

Here we experimentally realize topological phases with purely dissipative couplings. In contrast to previous works, our dissipatively coupled topological lattices exhibit topologically non-trivial bands of dissipation rates and feature robust topological edge states with dissipation rates between those of the bulk bands.

Our experimental platform consists of a time-multiplexed resonator network (Fig. 1b,c) that uses the notion of synthetic dimensions[29,30] to generate dissipatively coupled lattices that are capable of hosting non-trivial topological invariants. A general implementation of this network (Fig. 1b) contains $N$ resonant optical pulses separated by repetition period $T_R$. Each pulse represents a single, synthetic lattice site, represented by a synthetic resonator (Fig. 1c).

[1]Department of Applied Physics, California Institute of Technology, Pasadena, CA, USA. [2]Department of Electrical Engineering, Stanford University, Stanford, CA, USA. [3]Department of Mechanical Engineering and IPST, University of Maryland, College Park, MD, USA. [4]Department of Electrical Engineering, California Institute of Technology, Pasadena, CA, USA. [5]State Key Laboratory of Advanced Optical Communication Systems and Networks, School of Physics and Astronomy, Shanghai Jiao Tong University, Shanghai, China. [6]Theoretical Quantum Physics Laboratory, RIKEN Cluster for Pioneering Research, Wako, Japan. [7]Department of Physics, University of Michigan, Ann Arbor, MI, USA. [8]RIKEN Center for Quantum Computing, Wako, Saitama, 351-0198, Japan. [9]These authors contributed equally: Christian Leefmans, Avik Dutt. ✉e-mail: marandi@caltech.edu

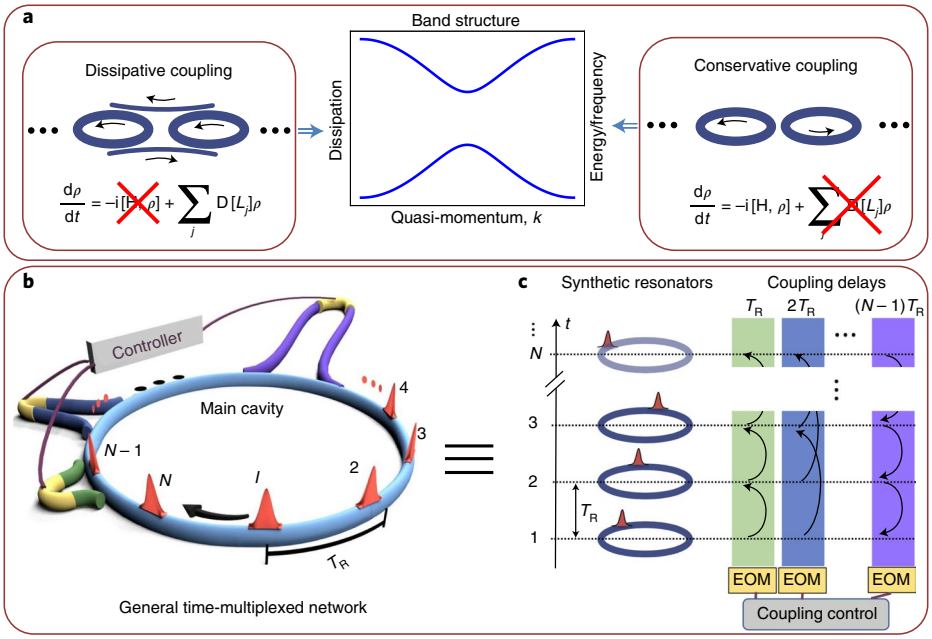


**Fig. 1 | Topological dissipation and time-multiplexed resonator networks. a**, Dissipatively coupled resonators (left) can map the energy spectrum of a tight-binding model to the dissipation spectrum of the resonators. The dynamics of dissipatively coupled resonators can be described by the dissipators $\mathcal{D}[L_j]$ of a Lindblad master equation (equation (1)). Note that with purely dissipative couplings, there are no Hamiltonian dynamics ($\mathcal{H}=0$) (Supplementary Section 5 provides a detailed derivation). On the other hand, conservatively coupled resonators (right) map the energy bands of a tight-binding model to the frequency spectrum of the resonators. In the absence of loss, the dynamics of a conservatively coupled system exhibit only Hamiltonian dynamics: $\dot{\rho} = -i[\mathcal{H}, \rho]$. **b**, Schematic of a resonant cavity loop (light blue) that supports $N$ pulses separated by a repetition period, $T_R$, and possesses delay lines of various lengths. The delay lines contain EOMs (yellow) that are driven by a controller. **c**, Equivalent synthetic resonator representation of **b**. Each synthetic resonator consists of a single, recirculating pulse. The time-multiplexed network is built by coupling the pulses with delay lines, which are indicated by the shaded boxes.

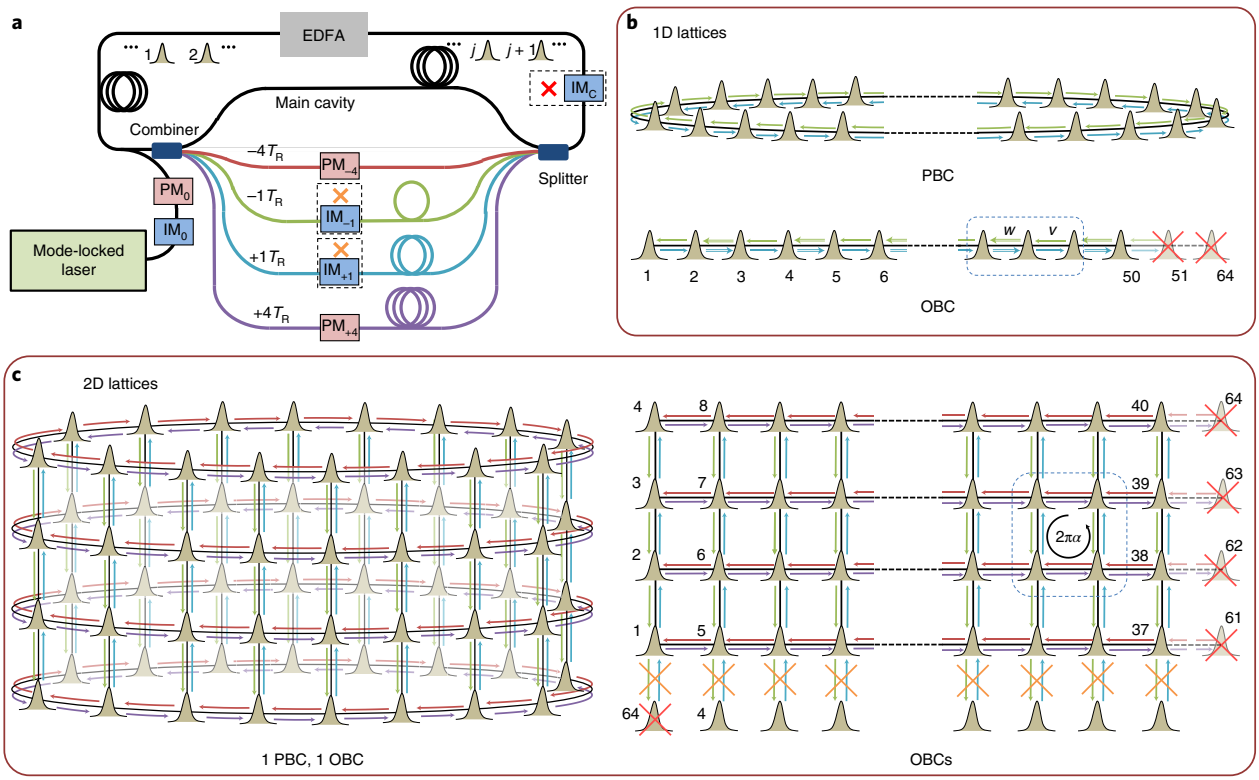


**Fig. 2 | Realizing 1D and 2D synthetic lattices with switchable boundary conditions in a time-multiplexed resonator network. a**, We construct a four-delay-line, time-multiplexed network capable of implementing two synthetic dimensions. An erbium-doped fiber amplifier (EDFA) partially compensates for the roundtrip loss in the network. **b**, With the $\pm 4T_R$ delay lines blocked, we use IMs in the $\pm T_R$ delay lines, namely, $IM_{\pm 1}$, to implement a 1D chain with staggered couplings ($w$ and $v$) of the SSH model. The intracavity IM, namely, $IM_C$, enables both PBCs and OBCs. **c**, With all four delay lines, the network can implement a 2D square lattice. The PMs in the $\pm 4T_R$ delay lines, namely, $PM_{\pm 4}$, produce the time-reversal symmetry-breaking couplings of the HH model, whereas $IM_{\pm 1}$ enforces OBCs along the 'vertical' direction. $IM_C$ enables PBCs or OBCs along the 'horizontal' direction.

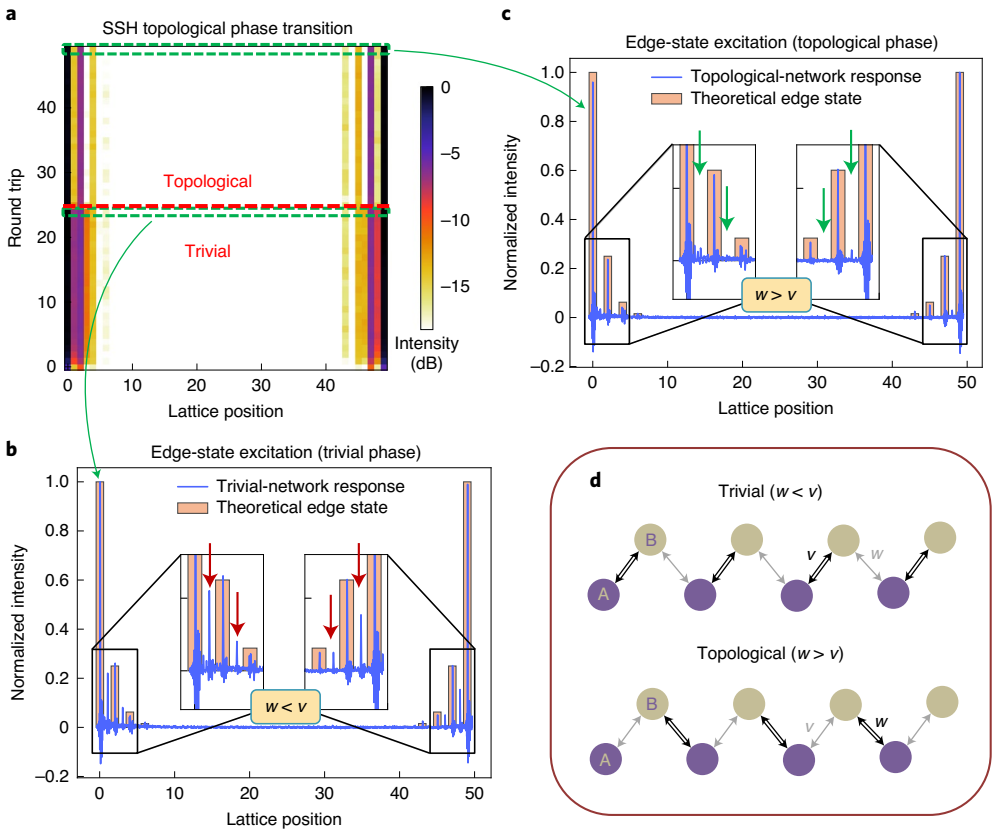


**Fig. 3 | Observations of the SSH edge state and topological phase transition. a**, For 50 round trips, we excite the SSH edge state corresponding to a coupling ratio of $w/v=2$ in our time-multiplexed network as we tune the delay-line couplings to induce a topological phase transition between the trivial and topological phases of the SSH model. **b**, For the first 25 round trips, we set the network coupling ratio to the trivial phase ($w/v=1/2$), and we observe that the edge state diffuses away from the edge as it resonates in the network (indicated by the thick red arrows). **c**, After 25 round trips, we switch the coupling ratio to the topological phase ($w/v=2$). The strong localization of the edge state in the topological phase (indicated by the thick green arrows) suggests that the edge state is an eigenstate of the network and corroborates our observation of a dynamic topological phase transition. **d**, Depictions of the SSH lattice corresponding to the trivial and topological phases.

As the pulses traverse the primary fibre loop (main cavity; Fig. 1b), a portion of each pulse enters the network's $(N-1)$ delay lines. These delay lines act analogously to the bus waveguides in Fig. 1a by mediating unidirectional couplings between the network's time-multiplexed resonators. The lengths of the $(N-1)$ delay lines are chosen so that each pulse couples to the other $(N-1)$ pulses in the network, and the electro-optic modulators (EOMs) in the delay lines determine the strengths and phases of the couplings[13]. By mapping the couplings of the network to a particular lattice model, our network represents the connections of the model under study.

Although previous studies have realized time-multiplexed random walks in synthetic photonic lattices[26,31–33], these travelling-wave architectures relied on conservatively coupled fibre loops and functioned like real-space waveguide arrays. Moreover, it has not been shown how to extend these architectures beyond the nearest-neighbour coupling or to higher than two dimensions. In contrast, the flexible site-to-site couplings of our resonator-based design are akin to those of the original optical Ising machine[13], and furthermore, by simply adding more delay lines, it is straightforward to realize long-range couplings, different lattice types and additional synthetic dimensions with our network architecture. In addition, our network may be reconfigured to realize different lattice models or different parameter regimes by reprogramming the modulator driving signals that control the strengths and phases of the couplings. In this work, we demonstrate our network's ability to readily implement multiple synthetic dimensions, tunable boundary conditions, dynamic and inhomogeneous couplings, and time-reversal symmetry-breaking gauge potentials. Simultaneously achieving these behaviours presents a substantial challenge to existing platforms for synthetic dimensions[29,30,34,35]. Furthermore, the dissipation introduced by our system's dissipative couplings stands in sharp contrast to the on-site gain and loss used to realize non-Hermitian topology[36,37] or non-reciprocal couplings in previous, conservatively coupled experiments[26]. It is our dissipative couplings that give rise to topologically non-trivial bands of dissipation rates in our system and that distinguish our work from previous works on topological photonics.

To study the dissipatively coupled equivalents of the Su–Schrieffer–Heeger (SSH)[38] and Harper–Hofstadter (HH)[39,40] models, we construct a four-delay-line network (Fig. 2a) that hosts $N=64$ synthetic lattice sites and can implement one-dimensional (1D) chains and two-dimensional (2D) square lattices either with open boundary conditions (OBCs) or with periodic boundary conditions (PBCs) along one dimension (Fig. 2b,c). The details of this setup are described in Supplementary Section 1. We model the dynamics of this network by the general Lindblad master equation

$$\frac{\mathrm{d}}{\mathrm{d}t}\rho = \mathcal{L}\rho = -\mathrm{i}\left[\mathcal{H}, \rho\right] + \sum_j \mathcal{D}\left[L_j\right]\rho. \quad (1)$$

Here $\mathcal{H}$ denotes the Hermitian Hamiltonian dynamics due to conservative couplings between sites labelled by $j$ (Fig. 1a, right).

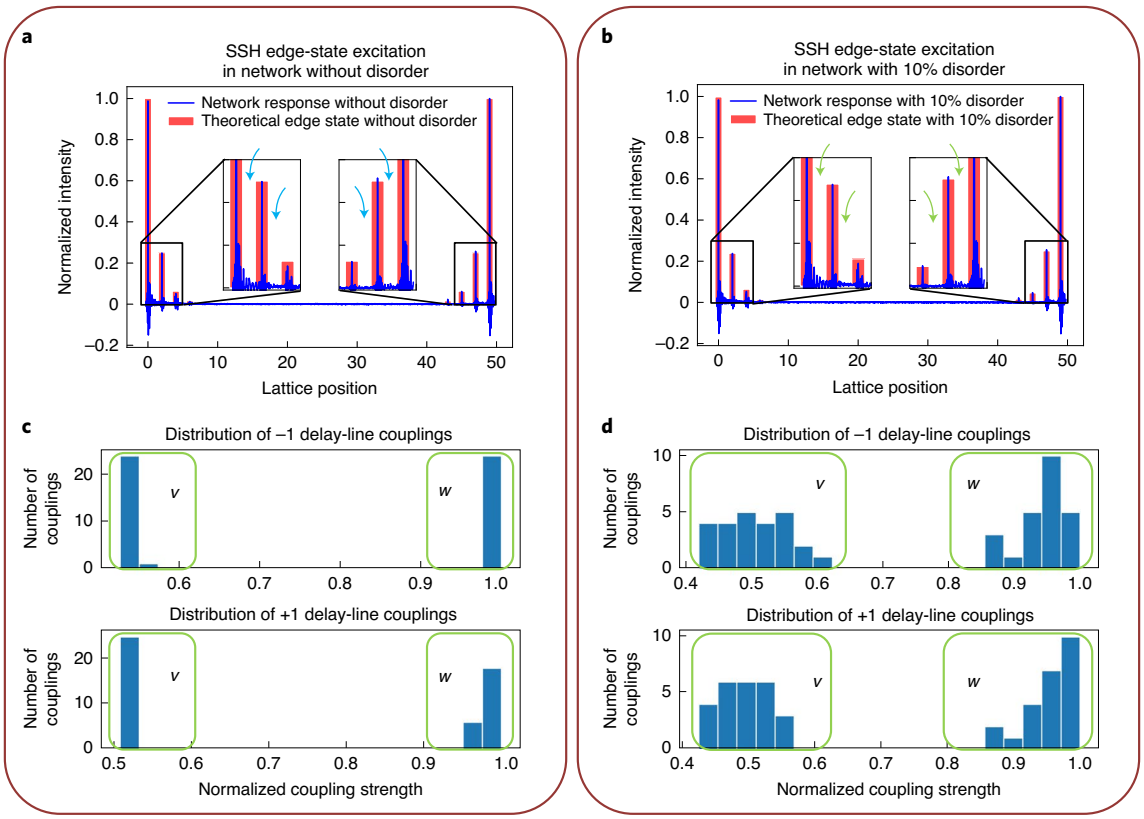


**Fig. 4 | Robustness of the dissipative SSH edge state and its quality factor. a**, Measured SSH edge state in a lattice without intentional disorder. **b**, Measured SSH edge state in the presence of disorder. In the presence of chiral-symmetry-preserving disorder, the SSH edge state persists, despite the slight change in the eigenstate. Furthermore, we expect the dissipation rate of the edge state to be unchanged, which is a hallmark of topological protection in our dissipatively coupled SSH lattice. We verify the robustness of the dissipation rate and the quality factor of the edge state by measuring the total intensities of the unperturbed and the disordered steady states of the network, which, under our experimental conditions, allows a comparison equivalent to comparing the dissipation rates. **c**, Distribution of the measured coupling strengths in the unperturbed lattice. Here the variation in the couplings is due to experimental imperfections ($w$ is the inter-dimer coupling; $v$ is the intra-dimer coupling). **d**, Distribution of the measured coupling strengths in the disordered lattice. We add disorder to each coupling that is drawn from the uniform distribution Unif(–0.1$w$, 0.1$w$). Comparing **c** and **d** suggests that the additional disorder is considerably stronger than the disorder introduced by experimental imperfections.

Because our network possesses purely dissipative couplings (Fig. 1a, left), we consider the case in which $\mathcal{H}=0$. Instead, the dissipators $D[L_j]\rho = L_j\,\rho L_j^\dagger - \{L_j^\dagger L_j,\,\rho\}/2$, with jump operators $L_j = \sqrt{\Gamma}\left(a_j + \mathrm{e}^{-\mathrm{i}\theta}a_{j+1}\right)$, completely describe the dissipative couplings between our synthetic lattice sites[16]. Here $\Gamma$ represents a dissipative coupling rate, and $\theta$ is related to the coupling phases. In Supplementary Section 5, we derive the jump operators for our network's delay-line architecture (Fig. 1b) and show how to implement dissipatively coupled SSH and HH lattices. We also show how to engineer the phases of the delay lines to emulate purely conservative and hybrid conservative–dissipative dynamics with our network's dissipative couplings. Although our current experimental results can be explained by the classical, mean-field behaviour of equation (2) (as discussed below), the full quantum dynamics of equation (1) may be applicable to future implementations with lower intrinsic losses and greater nonlinearities. In this sense, our work represents a step towards the experimental realization of photonic topological open quantum systems, where there is an i nteresting interplay between the dark states, quantum jumps and topology[17,27,41].

Starting from equation (1), we can express the evolution of the mean-field pulse amplitudes $a_j$ as

$$\frac{\mathrm{d}\mathbf{a}}{\mathrm{d}t} = (K-\gamma)\mathbf{a} + \mathbf{P}, \qquad (2)$$

where $t$ represents the slow-time (round-trip-to-round-trip) evolution of the network, $\gamma$ represents the intrinsic losses of resonators, $\mathbf{P}$ models a coherent drive and $K$ is the network's coupling matrix. Notably, our time-multiplexed resonator network can implement arbitrary amplitudes and phases for the coupling matrix elements $K_{mn}$ without any symmetry constraints. This is substantially beyond the capabilities of previous synthetic-dimensional architectures—either other time-multiplexed systems[26,31–33] or architectures that utilize alternative synthetic dimensions[20,34,35,42]. By engineering $K$ to implement the couplings of the SSH or HH model, our dissipatively coupled network acquires a dissipation spectrum identical to the topologically non-trivial band structure of the model under study. Moreover, the mean-field eigenstates of equation (2) also become the eigenstates of the model implemented by $K$. As the topological invariants of the SSH and HH models depend solely on the models' eigenstates, the topological invariants of our dissipatively coupled network are, therefore, identical to those of the familiar, conservatively coupled systems; however, the topological invariants are now associated with topologically non-trivial dissipation bands (Supplementary Section 4). As a result, in the presence of OBCs, our network is guaranteed to possess the same topological edge states as its conservatively coupled counterparts, and the edge states inherit the same robustness against disorder in the system (Supplementary Section 4).

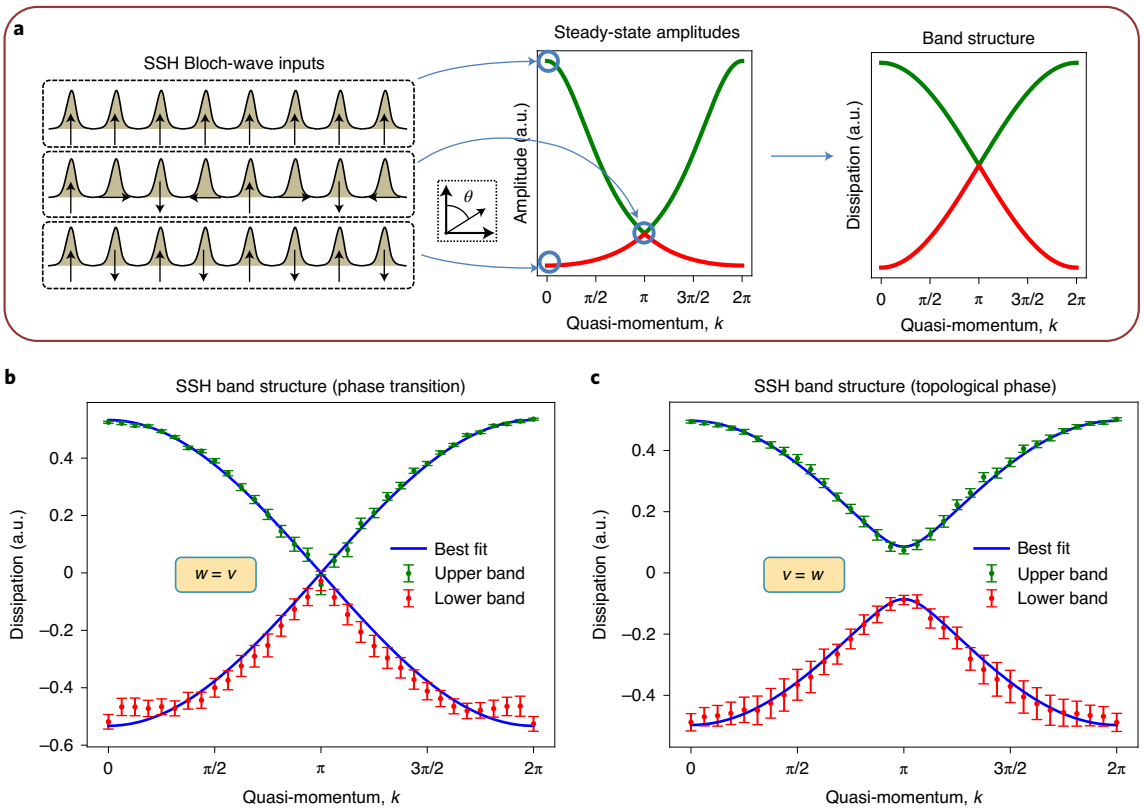


**Fig. 5 | Measurements of the SSH band structure. a**, To measure the SSH band structure at a given coupling ratio $w/v$, we excite the complete set of Bloch-wave eigenstates in the network and measure the steady-state amplitude of each state. Using equation (2), we transform these amplitudes into the SSH band structure. **b**,**c**, Measurements of the SSH band structure at the phase transition point (**b**) and topological phase (**c**). Using the best-fit curves, we extract the coupling ratios for each measurement. We measure $w/v \approx 1.0$ (expected $w/v = 1$) and $w/v \approx 1.4$ (expected $w/v = \sqrt{2} \approx 1.414$) for the measurements in **b** and **c**, respectively. Note that the error bars represent the standard errors of five measurements at each quasi-momentum.

Introducing a properly engineered coherent drive into our network (**P** in equation (2)) allows us to probe the specific states in our dissipative topological lattice. We generate the desired **P** by using the modulators $IM_0$ and $PM_0$ in Fig. 2a to excite a specific state of the network, and we track the state's evolution to acquire information about the underlying synthetic lattice. For instance, to probe the network's topological edge state, we program **P** to excite the edge state. If the edge state is an eigenstate of the network, then the edge-state excitation will remain localized as it resonates within the network. On the other hand, if the edge state is not an eigenstate, then the edge-state excitation will undergo diffusive dynamics dictated by equation (2). Similarly, when we institute the network's single PBC, we can choose **P** to excite a lattice's complete set of Bloch eigenstates. Measuring the steady states of these eigenstates allows us to reconstruct the 1D band structure of the model under study (Supplementary Section 2).

To demonstrate purely dissipative topological phenomena, we first program our network to implement the couplings of the SSH model[38,43]. The SSH model describes a 1D dimerized chain with intra-dimer coupling $v$ and inter-dimer coupling $w$ (Fig. 3)[44], and the model's band structure is characterized by a topological winding number $\mathcal{W}$. When $w < v$, $\mathcal{W} = 0$, and the system is in a topologically trivial phase. However, when $w > v$, $\mathcal{W} = 1$, and the system is in a topological phase that hosts mid-gap, topologically protected edge states.

We probe the SSH model's topological edge state by implementing a 50 site SSH lattice with OBCs and by inducing a topological phase transition between the SSH model's trivial and topological phases (Fig. 3a). In addition to allowing us to probe the SSH model's trivial and topological phases in a single experiment, this measurement highlights our network's ability to implement dynamic couplings. For 50 round trips, we excite the network with the SSH edge state corresponding to the coupling ratio $w/v = 2$. For the first 25 round trips, we prepare our SSH lattice in the trivial phase by setting the coupling ratio of the network to $w/v = 1/2$; for the remaining 25 round trips, we switch the synthetic lattice into the topological phase by changing the coupling ratio to $w/v = 2$. As shown in Fig. 3b, when the lattice's couplings are in the trivial phase, the edge-state excitation diffuses into the initially unoccupied states of the lattice. In contrast, when the couplings are in the topological phase, the edge-state excitation remains strongly localized in the theoretically predicted edge state (Fig. 3c). This localization confirms the existence of a purely dissipative topological edge state in our time-multiplexed resonator network.

We next investigate the robustness of the dissipative SSH edge state in the presence of disorder in the couplings of the network. In Fig. 4, we show the measured resonant steady states in a network without coupling disorder (Fig. 4a,c) and in a network with additional coupling disorder drawn from $\mathrm{Unif}(-0.1w, 0.1w)$ (Fig. 4b,d). As discussed in Supplementary Section 4, in the presence of such chiral-symmetry-preserving disorder, we expect the dissipation rate of the disordered edge state to be identical to that of the edge state in the unperturbed system. This corresponds to topological robustness of the quality factor of the dissipative topological edge mode. We verify this robustness by measuring the total intensities ($I$; sum of the peak powers) in measurements of the edge state with and without

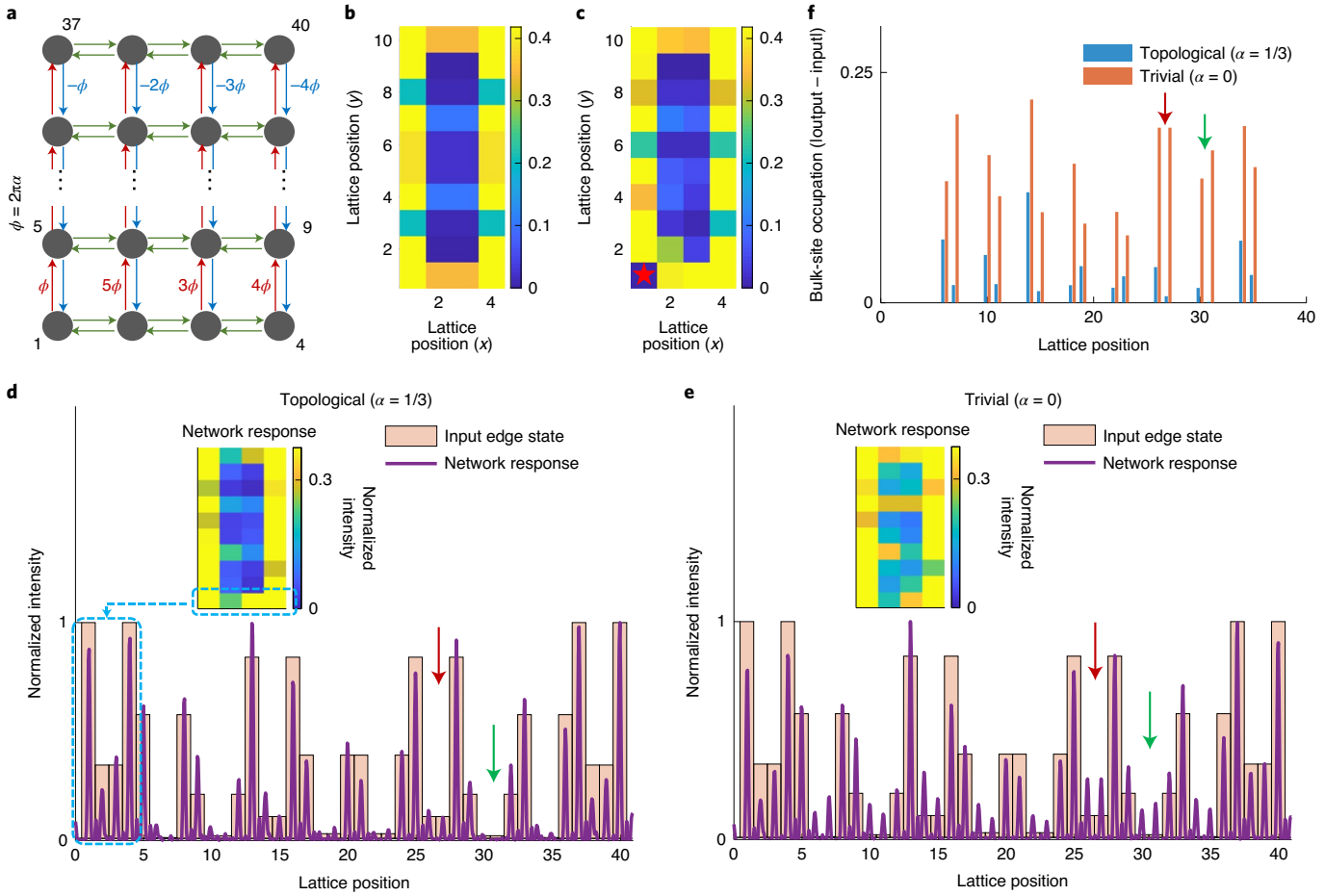


**Fig. 6 | Measurement of the HH edge state and its localization. a**, Schematic of the HH model with a magnetic flux of $\phi = 2\pi\alpha$ per plaquette. The horizontal couplings do not have any phase, whereas the vertical couplings implement the Peierls phases $\phi$, $2\phi$,... (red) and $-\phi$, $-2\phi$,... (blue). **b**, Simulated steady state of a theoretical HH edge state in a 4×10 dissipatively coupled lattice. The same edge state is studied in our experiments. **c**, Simulated steady state of an HH edge state in a 4×10 dissipatively coupled lattice with a corner defect. The new edge state wraps around the defect, demonstrating the robustness of the topological edge state in a dissipatively coupled lattice. **d**,**e**, Time traces of the measured steady-state pulse amplitudes in the network. As indicated by the dashed blue arrow in **d**, each set of four pulses maps to one row in the inset colour map, with earlier pulses in the time traces corresponding to lower rows in the colour maps. **d**, When the delay-line PMs implement the coupling phases of the HH model with $\alpha = 1/3$, the edge state is an eigenstate of the network, and it resonates in the system. **e**, When we turn off these coupling phases to achieve $\alpha = 0$, the edge state no longer resonates in the network. In particular, notice that light leaks into the 'bulk' in the time trace of this measurement. **f**, Difference between the bulk-site occupation for the topological case (blue) and trivial case (orange). The thick red and green arrows in **d**–**f** indicate the bulk sites with the highest contrast between the topological and trivial cases. Note that the presence of edge occupation that is visually apparent in **e** arises from the input excitation being predominantly localized on the edge (shaded rectangles), and hence, the contrast of bulk occupation in **f** provides a better comparison between the trivial and topological phases. Furthermore, note that the colour maps in **b**–**e** are saturated to emphasize the contrast between the edges and bulk.

disorder. Under the right experimental conditions, this comparison is equivalent to comparing the dissipation rates (Methods). In the unperturbed system, we find $I_{\mathrm{unpert}} = 0.377 \pm 0.001$ V, whereas in the disordered system, we find $I_{\mathrm{dis}} = 0.378 \pm 0.001$ V. The agreement between these two measurements provides strong evidence that the dissipation rate (and consequently the quality factor) of the SSH edge state is protected against the presence of chiral-symmetry-preserving disorder in the network.

Next, we experimentally reconstruct the dissipation bands of our SSH lattice in the topological phase ($w/v = \sqrt{2}$) and at the phase transition point ($w/v = 1$). For both coupling ratios, we implement a 64 site SSH lattice with PBCs. In each case, we sequentially excite the network with each of its 64 Bloch eigenstates, and we measure the steady-state amplitude of each state. Then, using the fit procedure described in Supplementary Section 2B, we extract the dissipation spectra from the measured steady-state amplitudes (Fig. 5b,c). To evaluate the quality of our band structure measurements, we compare the coupling ratios, $w/v$, extracted from our fit procedure with the expected coupling ratios. This comparison provides a suitable metric for the quality of our measurements because, up to a constant, the SSH coupling ratio completely determines the band structure[43]. For the band structure at the phase transition point (expected $w/v = 1$), we measure $w/v \approx 1.0$, whereas, for the band structure in the topological phase (expected $w/v = \sqrt{2} \approx 1.414$), we find $w/v \approx 1.4$. The excellent agreement between the measured band structures and our theoretical predictions confirms that our network possesses a topologically non-trivial dissipation spectrum.

Finally, to showcase the scalability and flexibility of our time-multiplexed network architecture, we reconfigure our synthetic lattice to probe the topological edge state of the HH model. The HH model describes a 2D square lattice subjected to a perpendicular magnetic field[3,39,40], whose strength is characterized by a dimensionless magnetic-field parameter $\alpha$. For rational $\alpha$, the bands of the HH model acquire a non-zero topological invariant

known as the Chern number $\mathcal{C}$, which gives rise to topologically protected edge states[5]. In our network, we use the modulators $PM_{\pm 4}$ (Fig. 2a) to achieve an effective magnetic field with $\alpha = 1/3$ in a $4 \times 10$ synthetic HH lattice with OBCs (Fig. 6a). Because the dissipative couplings of our network are time-modulated and unidirectional, the synthetic magnetic field generated by the delay lines breaks time-reversal symmetry—meaning that our network possesses truly nonzero Chern numbers (Supplementary Section 6). This is in stark contrast with earlier optical implementations of the HH model, which either do not break time-reversal symmetry[45] or only break $z$-reversal symmetry[46].

As shown in Fig. 6d, when we excite a topologically protected edge state of the HH model in the presence of the synthetic magnetic field, the edge state remains well localized. Interestingly, this edge state is strongly localized at the edges of the $4 \times 10$ lattice, despite only two bulk sites separating the edges along the narrow direction. On the other hand, when we excite the edge state in the absence of the synthetic magnetic field ($\alpha = 0$), the lattice represents a trivial insulator, and the edge state diffuses into the 'bulk' of the synthetic lattice (Fig. 6e). As the initial edge-state excitation is prominent in the responses of both topological and trivial networks (Fig. 6d,e), we plot only the occupation in the bulk sites (Fig. 6f) to clearly show that the edge state remains localized in the topological phase but not in the trivial phase. We quantify this contrast between the trivial and topological phases by defining a bulk occupation fraction

$$f_{\mathrm{bulk}} = \sum_{n_x, n_y \in \mathrm{bulk}} \left| \psi_{n_x, n_y} \right|^4,$$

subject to the normalization

$$\sum_{n_x, n_y} \left| \psi_{n_x, n_y} \right|^2 = 1.$$

We calculate $f_{\mathrm{bulk}}^{\mathrm{topo}} = 5.6 \times 10^{-4}$ and $f_{\mathrm{bulk}}^{\mathrm{triv}} = 2.2 \times 10^{-3}$ for the topological and trivial phases, respectively. As our $4 \times 10$ lattice has 16 bulk sites and 24 edge sites, $f_{\mathrm{bulk}}^{\mathrm{triv}} / f_{\mathrm{bulk}}^{\mathrm{topo}} \approx 4$ indicates considerably stronger penetration into the bulk for the lattice in the trivial phase. Based on this observation, we conclude that our time-multiplexed synthetic HH lattice hosts a multidimensional topological edge state.

From the non-trivial topology of the dissipatively coupled HH model's dissipation bands, we expect that the topological edge states of dissipative HH lattices should be robust against the effects of defects and disorder. We demonstrate this robustness by simulating the evolution of a $4 \times 10$ dissipatively coupled HH lattice with and without a defect added to one corner of the lattice. The results of these simulations are shown in Fig. 6b,c. In both cases, we find that when we excite the dissipative HH lattice with one of its topological edge states, the edge state remains localized in the initial excitation. For the dissipative HH lattice with a corner defect (Fig. 6c), this is a clear manifestation of topological protection. The details of these simulations are discussed in Supplementary Section 8.

Our dissipatively coupled implementations of the 1D SSH model and 2D HH model experimentally demonstrate the existence of topological phenomena in the presence of purely dissipative couplings. We leverage our time-multiplexed network's dissipative dynamics for edge state and band structure measurements, and we utilize the time-reversal symmetry-breaking nature of our dissipative couplings to introduce nonzero Chern numbers. Our time-multiplexed resonator architecture also offers a promising platform for future work in synthetic dimensions. Our design can be extended to lattices in higher than two dimensions[47–51] and to lattices with long-range couplings[42], can achieve dense connectivity between lattice sites, and can realize dynamic and inhomogeneous synthetic gauge fields[52]—a combination that is not easy to achieve with other experimental platforms. We anticipate that dissipative couplings will enable new topological devices with applications to quantum computing and photonics. Immediate extensions of our current experiments include exploring non-Hermitian[53,54] and nonlinear[55] topological behaviours in dissipatively coupled time-multiplexed networks.

## Online content

Any methods, additional references, Nature Research reporting summaries, source data, extended data, supplementary information, acknowledgements, peer review information; details of author contributions and competing interests; and statements of data and code availability are available at https://doi.org/10.1038/s41567-021-01492-w.

Received: 13 July 2021; Accepted: 10 December 2021;
Published online: 14 February 2022

## References

1. Hasan, M. & Kane, C. Colloquium: topological insulators. *Rev. Mod. Phys.* **82**, 3045 (2010).
2. Cooper, N., Dalibard, J. & Spielman, I. Topological bands for ultracold atoms. *Rev. Mod. Phys.* **91**, 015005 (2019).
3. Ozawa, T. et al. Topological photonics. *Rev. Mod. Phys.* **91**, 015006 (2019).
4. Jackiw, R. & Rebbi, C. Solitons with fermion number 1/2. *Phys. Rev. D* **13**, 3398 (1976).
5. Hatsugai, Y. Chern number and edge states in the integer quantum Hall effect. *Phys. Rev. Lett.* **71**, 3697–3700 (1993).
6. Metelmann, A. & Clerk, A. Nonreciprocal photon transmission and amplification via reservoir engineering. *Phys. Rev. X* **5**, 021025 (2015).
7. Mukherjee, S. et al. Dissipatively coupled waveguide networks for coherent diffusive photonics. *Nat. Commun.* **8**, 1909 (2017).
8. Ding, J., Belykh, I., Marandi, A. & Miri, M.-A. Dispersive versus dissipative coupling for frequency synchronization in lasers. *Phys. Rev. Appl.* **12**, 054039 (2019).
9. Barreiro, J. T. et al. An open-system quantum simulator with trapped ions. *Nature* **470**, 486–491 (2011).
10. Haus, H. Mode-locking of lasers. *IEEE J. Sel. Topics Quantum Electron.* **6**, 1173–1185 (2000).
11. Wright, L. G. et al. Mechanisms of spatiotemporal mode-locking. *Nat. Phys.* **16**, 565–570 (2020).
12. Verstraete, F., Wolf, M. M. & Cirac, J. I. Quantum computation and quantum-state engineering driven by dissipation. *Nat. Phys.* **5**, 633–636 (2009).
13. Marandi, A., Wang, Z., Takata, K., Byer, R. L. & Yamamoto, Y. Network of time-multiplexed optical parametric oscillators as a coherent Ising machine. *Nat. Photon.* **8**, 937–942 (2014).
14. Inagaki, T. et al. A coherent Ising machine for 2000-node optimization problems. *Science* **354**, 603–606 (2016).
15. Fang, K. et al. Generalized non-reciprocity in an optomechanical circuit via synthetic magnetism and reservoir engineering. *Nat. Phys.* **13**, 465–471 (2017).
16. Wanjura, C. C., Brunelli, M. & Nunnenkamp, A. Topological framework for directional amplification in driven-dissipative cavity arrays. *Nat. Commun.* **11**, 3149 (2020).
17. Gneiting, C., Koottandavida, A., Rozhkov, A. V. & Nori, F. Unraveling the topology of dissipative quantum systems. Preprint at https://arxiv.org/abs/2007.05960 (2020).
18. Dasbiswas, K., Mandadapu, K. K. & Vaikuntanathan, S. Topological localization in out-of-equilibrium dissipative systems. *Proc. Natl Acad. Sci. USA* **115**, E9031–E9040 (2018).
19. Li, M., Ni, X., Weiner, M., Alù, A. & Khanikaev, A. B. Topological phases and nonreciprocal edge states in non-Hermitian Floquet insulators. *Phys. Rev. B* **100**, 045423 (2019).
20. Wang, K. et al. Generating arbitrary topological windings of a non-Hermitian band. *Science* **371**, 1240–1245 (2021).
21. Mukherjee, S. & Rechtsman, M. C. Observation of Floquet solitons in a topological bandgap. *Science* **368**, 856–859 (2020).
22. Maczewsky, L. et al. Nonlinearity-induced photonic topological insulator. *Science* **370**, 701–704 (2020).
23. Xia, S. et al. Nonlinear tuning of PT-symmetry and non-Hermitian topological states. *Science* **372**, 72–76 (2021).

24. Zhao, H. et al. Topological hybrid silicon microlasers. *Nat. Commun.* **9**, 981 (2018).
25. Zhao, H. et al. Non-Hermitian topological light steering. *Science* **365**, 1163–1166 (2019).
26. Weidemann, S. et al. Topological funneling of light. *Science* **368**, 311–314 (2020).
27. Bardyn, C.-E. et al. Topology by dissipation. *New J. Phys.* **15**, 085001 (2013).
28. Yoshida, T. & Hatsugai, Y. Bulk edge correspondence of classical diffusion phenomena. *Sci. Rep.* **11**, 888 (2021).
29. Ozawa, T. & Price, H. Topological quantum matter in synthetic dimensions. *Nat. Rev. Phys.* **1**, 349–357 (2019).
30. Yuan, L., Lin, Q., Xiao, M. & Fan, S. Synthetic dimension in photonics. *Optica* **5**, 1396–1405 (2018).
31. Wimmer, M., Price, H., Carusotto, I. & Peschel, U. Experimental measurement of the Berry curvature from anomalous transport. *Nat. Phys.* **13**, 545–550 (2017).
32. Chen, C. et al. Observation of topologically protected edge states in a photonic two- dimensional quantum walk. *Phys. Rev. Lett.* **121**, 100502 (2018).
33. Chalabi, H. et al. Synthetic gauge field for two-dimensional time-multiplexed quantum random walks. *Phys. Rev. Lett.* **123**, 150503 (2019).
34. Lustig, E. et al. Photonic topological insulator in synthetic dimensions. *Nature* **567**, 356–360 (2019).
35. Dutt, A. et al. A single photonic cavity with two independent physical synthetic dimensions. *Science* **367**, 59–64 (2020).
36. Zeuner, J. et al. Observation of a topological transition in the bulk of a non-Hermitian system. *Phys. Rev. Lett.* **115**, 040402 (2015).
37. Weimann, S. et al. Topologically protected bound states in photonic parity–time-symmetric crystals. *Nat. Mater.* **16**, 433–438 (2017).
38. Su, W. P., Schrieffer, J. R. & Heeger, A. J. Solitons in polyacetylene. *Phys. Rev. Lett.* **42**, 1698–1701 (1979).
39. Hofstadter, D. Energy levels and wave functions of Bloch electrons in rational and irrational magnetic fields. *Phys. Rev. B* **14**, 2239–2249 (1976).
40. Harper, P. G. The general motion of conduction electrons in a uniform magnetic field, with application to the diamagnetism of metals. *Proc. Phys. Soc. A* **68**, 879 (1955).
41. Diehl, S., Rico, E., Baranov, M. A. & Zoller, P. Topology by dissipation in atomic quantum wires. *Nat. Phys.* **7**, 971–977 (2011).
42. Bell, B. A. et al. Spectral photonic lattices with complex long-range coupling. *Optica* **4**, 1433–1436 (2017).
43. Asbóth, J., Oroszlány, L. & Pályi, A. *A Short Course on Topological Insulators* 1st edn (Springer, 2016).
44. Malkova, N., Hromada, I., Wang, X., Bryant, G. & Chen, Z. Observation of a topological transition in the bulk of a non-Hermitian system. *Phys. Rev. Lett.* **115**, 040402 (2015).
45. Hafezi, M., Mittal, S., Fan, J., Migdall, A. & Taylor, J. M. Imaging topological edge states in silicon photonics. *Nat. Photon.* **7**, 1001–1005 (2013).
46. Rechtsman, M. C. et al. Photonic Floquet topological insulators. *Nature* **496**, 196–200 (2013).
47. Zhang, S.-C. & Hu, J. A four-dimensional generalization of the quantum Hall effect. *Science* **294**, 823–828 (2001).
48. Petrides, I., Price, H. M. & Zilberberg, O. Six-dimensional quantum Hall effect and three-dimensional topological pumps. *Phys. Rev. B* **98**, 125431 (2018).
49. Lohse, M., Schweizer, C., Price, H. M., Zilberberg, O. & Bloch, I. Exploring 4D quantum Hall physics with a 2D topological charge pump. *Nature* **553**, 55–58 (2018).
50. Zilberberg, O. et al. Photonic topological boundary pumping as a probe of 4D quantum Hall physics. *Nature* **553**, 59–62 (2018).
51. Wang, K. et al. Multidimensional synthetic chiral-tube lattices via nonlinear frequency conversion. *Light Sci. Appl.* **9**, 132 (2020).
52. Fang, K. & Fan, S. Controlling the flow of light using the inhomogeneous effective gauge field that emerges from dynamic modulation. *Phys. Rev. Lett.* **111**, 203901 (2013).
53. Helbig, T. et al. Generalized bulk-boundary correspondence in non-Hermitian topolectrical circuits. *Nat. Phys.* **16**, 747–750 (2020).
54. Parto, M., Liu, Y., Bahari, B., Khajavikhan, M. & Christodoulides, D. Non-Hermitian and topological photonics: optics at an exceptional point. *Appl. Phys. Rev.* **10**, 403–423 (2020).
55. Smirnova, D., Leykam, D., Chong, Y. & Kivshar, Y. Nonlinear topological photonics. *Appl. Phys. Rev.* **7**, 021306 (2020).

## Methods

**Network architecture.** The time-multiplexed optical network studied in this work hosts $N=64$ time-multiplexed resonators and possesses four delay lines, labelled $\pm T_R$ and $\pm 4T_R$ delay lines (Fig. 2a). Each delay line differs in length from the corresponding section in the main cavity by an integer multiple of the pulse repetition period $T_R$. The '−' ('+') indicates that the delay line is shorter (longer) than the corresponding main-loop section, and the accompanying number denotes the range of the coupling (for example, the $\pm 4T_R$ delay lines implement the fourth-nearest-neighbour coupling). As the separate $\pm NT_R$ delay lines provide independent control over each direction of the $N$th-nearest-neighbour couplings, it is straightforward to implement non-reciprocal couplings between sites.

The SSH model only requires nearest-neighbour coupling; therefore, to study the SSH model, we block the $\pm 4T_R$ delay lines. We then map the pulses in the main cavity to the 1D chain in Fig. 2b, where the colours of the couplings correspond to the colours of the delay lines that implement them. The intensity modulators (IMs) inserted in the $\pm T_R$ delay lines provide pulse-to-pulse control over the coupling strengths of each delay line and enable us to implement the staggered couplings of the SSH model. Moreover, although the topology of the main cavity lends itself to periodic boundary conditions (PBCs), the intra-cavity IM, namely, $IM_C$ (Fig. 2a), provides control over the boundaries of the synthetic 1D lattice. We can switch the boundary conditions to open boundary conditions (OBCs) simply by using $IM_C$ to suppress the time slots in the main cavity (Fig. 2b).

To realize the HH model in the network (Fig. 2a), we use the $\pm 4T_R$ delay lines to define the nearest-neighbour couplings along the second dimension of a synthetic square lattice[56]. By using the IMs in the $\pm T_R$ delay lines to suppress the 'spiralling' boundary condition along this second synthetic dimension, we arrive at the lattices shown in Fig. 2c, where, once again, $IM_C$ enables us to implement either a strip with a single PBC or a square lattice with OBCs. To achieve the time-reversal symmetry-breaking coupling phases of the HH model, we place phase modulators (PMs) in the $\pm 4T_R$ delay lines. We utilize our independent control over each delay line to introduce a synthetic magnetic flux in each plaquette of the synthetic lattice (Fig. 2c).

For the measurements presented in the main text, we probe the properties of the network by exciting states in the network and recording the network's steady-state response. To excite the desired edge states and Bloch-wave eigenstates, we use an IM ($IM_0$) and a PM ($PM_0$) at the input of the main cavity (Fig. 2a). These modulators encode the intensities and phases of the desired state onto a stream of pulses from a mode-locked laser. On entering the cavity, these pulses excite the sites of the synthetic lattice (that is, the time bins of the network) with particular amplitudes and phases. By repeatedly exciting each site over multiple round trips of the network, we bring the cavity to a resonant steady state.

**Measurement procedure.** *SSH band structure measurements.* To measure the SSH band structure, we generate the modulator driving signals to implement the desired coupling ratio within the network (using $IM_{\pm 1}$) and the Bloch-wave excitations at the input to the cavity (using $PM_0$). By not using $IM_C$, the network inherently implements PBCs; therefore, we implement a 64 pulse (32 dimer) SSH lattice.

To perform the experiment, we excite each Bloch eigenstate in the network and record the network's steady-state response to each state. We repeat this measurement five times for each Bloch wave and compile the data from the different measurements to generate a plot of the mean steady-state amplitudes versus the wavevector. We then solve equation (2) to relate the steady-state amplitudes of the Bloch waves, $|c(k)|^2$, to the dissipation eigenvalues of the SSH model. We find

$$|c(k)|^2 = \frac{A}{(\gamma - \lambda_{\mathrm{SSH}})^2} + d, \tag{3}$$

where $\gamma$ is the network loss; $\lambda_{\mathrm{SSH}} = \sqrt{w^2 + v^2 + 2wv\cos(k)}$; and $A$ and $d$ account for detector scaling and bias, respectively.

We fit the measured amplitudes with a rescaled version of equation (3) using Markov chain Monte Carlo (MCMC) simulations[57]. We use the fit parameters to transform the measured amplitudes into the SSH band structures shown in Fig. 5b,c.

*Edge-state measurements.* Our edge-state measurements follow a procedure similar to that used for our band structure measurements. To observe the HH model's edge state, we first generate modulator driving signals to implement the synthetic gauge field of the HH model (using $PM_{\pm 4}$) and to produce the HH edge state at the input to the network (using $IM_0$ and $PM_0$). As suggested in Fig. 2a,c, we use the delay-line IMs, namely, $IM_{\pm 1}$, to create OBCs along one direction of the lattice, whereas $IM_C$ produces OBCs along the other direction. The result is that we implement a finite, $4\times 10$ HH lattice with an effective synthetic magnetic field corresponding to $\alpha = 1/3$.

To probe the topologically non-trivial state of our lattice, we excite the HH edge state in the network and record the system's steady state. In the presence of the synthetic gauge field, the edge state is an eigenstate of the network; therefore, the excited edge state resonates unperturbed within the network. This result is shown in Fig. 6d.

To confirm that the lattice hosts a 2D topological edge state, we next turn off the synthetic gauge field by turning off the driving signals on $PM_{\pm 4}$. The network then implements a trivial $4\times 10$ square lattice. We excite the same topological edge state in the trivial lattice and observe that the network's steady-state response deviates from the edge-state excitation (Fig. 6e). This confirms that, in the presence of the synthetic gauge field, the topological edge state is an eigenstate of the network.

For the SSH model, we first observe the topological edge state in the context of a dynamical topological phase transition between the trivial and topological phases (Fig. 3a). We begin by generating the modulator driving signals to implement the SSH model's couplings and to excite the SSH edge state. In addition, we now use $IM_C$ to implement a 50 pulse SSH lattice with OBCs. We excite the SSH edge state in the network for 50 round trips. For the first 25 round trips, we program the couplings so that the network is in the trivial phase of the SSH model. In this case, we observe that the steady-state response of the network deviates from the excited edge state. For the final 25 round trips, we switch the coupling strengths so that the network is in the SSH model's topological phase. Now, we observe that the network response remains strongly localized in the edge state. This indicates that the topological edge state is an eigenstate of the network when the network is in the topological phase.

We investigate the robustness of the SSH edge state using a similar procedure. We first program the network's couplings to implement the SSH model with no disorder and then program the couplings to implement the SSH model with additional disorder distributed according to $\mathrm{Unif}(-0.1w, 0.1w)$. In each case, we perform the edge-state measurement 40 times and average the results. In both cases, we excite the network with the predicted SSH edge state for 15 round trips and record the steady state of the network on the 15th round trip.

Because we excite the network with eigenstates in the disordered and unperturbed cases, equation (2) again reduces to a scalar equation, and its solution can be written in the form

$$|c_{\mathrm{edge}}|^2 = \frac{A}{(\gamma - \lambda_{\mathrm{edge}})^2} + d, \tag{4}$$

which is very similar to equation (3), but it is now specialized to the case of the SSH edge state. During our calibration, we take care to ensure that the probed edge states have the same normalization in both the disordered and the unperturbed lattices so that the pump parameter ($A$ in equation (3)) is the same for both cases. Then, comparing the total intensities in the resonant steady states becomes equivalent to comparing the dissipation rates with and without disorder. We use this comparison to conclude that the dissipation rate of the dissipatively coupled SSH edge state is robust against the chiral-symmetry-preserving disorder introduced into the system.

Note that the time traces plotted in Figs. 3, 4 and 6 are normalized by rescaling the time trace by the maximum value in the averaged trace. The data plotted in the colour map shown in Fig. 3a is not normalized, and the reference level used to plot these data in units of decibels is the maximum intensity in the entire dataset.

## Data availability

The data used to generate the plots and results in this paper is available on the Caltech Research Data Repository (https://doi.org/10.22002/D1.2202). Source data are provided with this paper. All other data that support the findings of this study are available from the corresponding author upon reasonable request.

## Code availability

The code used to analyse and plot the data in this paper is available on the Caltech Research Data Repository (https://doi.org/10.22002/D1.2202). The other code supporting the findings of this study is available from the corresponding author upon reasonable request.

## References

56. Yuan, L., Xiao, M., Lin, Q. & Fan, S. Synthetic space with arbitrary dimensions in a few rings undergoing dynamic modulation. *Phys. Rev. B* **97**, 104105 (2018).
57. Aster, R. C., Borchers, B. & Thurber, C. H. *Parameter Estimation and Inverse Problems* 2nd edn (Elsevier Science and Technology, 2013).

## Acknowledgements

We are grateful to M. Fraser and A. Szameit for their insights. We acknowledge support from ARO grant no. W911NF-18-1-0285 and NSF grant nos. 1846273 and 1918549. S.F. acknowledges support of a Vannevar Bush Faculty Fellowship from the US Department of Defense (grant no. N00014-17-1-3030). L.Y. acknowledges support of the National Natural Science Foundation of China (11974245). F.N. acknowledges support from ARO (W911NF-18-1-0358), JST-CREST (JPMJCR1676), JSPS (JP20H00134), AOARD (FA2386-20-1-4069) and FQXi (FQXi-IAF19-06). We wish to thank NTT Research for their financial and technical support.

## Author contributions

C.L., A.D. and A.M. devised the experiments and the underlying theory. C.L., A.D. and J.W. constructed and performed the experiments. C.L. collected and analysed the data. M.P. contributed to the theoretical analysis. L.Y. conceived the experiment. S.F. and F.N. provided additional insights and guidance. All the authors discussed the results and contributed to the writing of the manuscript. A.M. supervised the project.

## Competing interests

The authors declare no competing interests.

## Additional information

**Supplementary information** The online version contains supplementary material available at https://doi.org/10.1038/s41567-021-01492-w.

**Correspondence and requests for materials** should be addressed to Alireza Marandi.

**Peer review information** *Nature Physics* thanks Yaakov Lumer and the other, anonymous, reviewer(s) for their contribution to the peer review of this work.

**Reprints and permissions information** is available at www.nature.com/reprints.